Projection-resolved optical coherence tomographic angiography

Miao Zhang, Thomas S. Hwang, J. Peter Campbell, Steven T. Bailey, David J. Wilson, David Huang and Yali Jia[*]

Casey Eye Institute, Oregon Health & Science University, Portland, OR 97239, USA
[*]*jiaya@ohsu.edu*

Abstract: Shadowgraphic projection artifacts from superficial vasculature interfere with the visualization of deeper vascular networks in optical coherence tomography angiography (OCT-A). We developed a novel algorithm to remove this artifact by resolving the ambiguity between *in situ* and projected flow signals. The algorithm identifies voxels with *in situ* flow as those where intensity-normalized decorrelation values are higher than all shallower voxels in the same axial scan line. This "projection-resolved" (PR) algorithm effectively suppressed the projection artifact on both *en face* and cross-sectional angiograms and enhanced depth resolution of vascular networks. In the human macula, the enhanced angiograms show three distinct vascular plexuses in the inner retina and no vessels in the outer retina. We demonstrate that PR OCT-A cleanly removes flow projection from the normally avascular outer retinal slab while preserving the density and continuity of the intermediate and deep retinal capillary plexuses.

References and links

1. Y. Jia, O. Tan, J. Tokayer, B. Potsaid, Y. Wang, J. J. Liu, M. F. Kraus, H. Subhash, J. G. Fujimoto, J. Hornegger, and D. Huang, "Split-spectrum amplitude-decorrelation angiography with optical coherence tomography," Opt. Express **20**(4), 4710–4725 (2012).
2. R. K. Wang, S. L. Jacques, Z. Ma, S. Hurst, S. R. Hanson, and A. Gruber, "Three dimensional optical angiography," Opt. Express **15**(7), 4083–4097 (2007).
3. S. Makita, F. Jaillon, M. Yamanari, M. Miura, and Y. Yasuno, "Comprehensive in vivo micro-vascular imaging of the human eye by dual-beam-scan Doppler optical coherence angiography," Opt. Express **19**(2), 1271–1283 (2011).
4. Y. Jia, S. T. Bailey, T. S. Hwang, S. M. McClintic, S. S. Gao, M. E. Pennesi, C. J. Flaxel, A. K. Lauer, D. J. Wilson, J. Hornegger, J. G. Fujimoto, and D. Huang, "Quantitative optical coherence tomography angiography of vascular abnormalities in the living human eye," Proc. Natl. Acad. Sci. U.S.A. **112**(18), E2395–E2402 (2015).
5. M. P. López-Sáez, E. Ordoqui, P. Tornero, A. Baeza, T. Sainza, J. M. Zubeldia, and M. L. Baeza, "Fluorescein-induced allergic reaction," Ann. Allergy Asthma Immunol. **81**(5), 428–430 (1998).
6. T. S. Hwang, Y. Jia, S. S. Gao, S. T. Bailey, A. K. Lauer, C. J. Flaxel, D. J. Wilson, and D. Huang, "Optical Coherence Tomography Angiography Features of Diabetic Retinopathy," Retina **35**(11), 2371–2376 (2015).
7. Y. Jia, S. T. Bailey, D. J. Wilson, O. Tan, M. L. Klein, C. J. Flaxel, B. Potsaid, J. J. Liu, C. D. Lu, M. F. Kraus, J. G. Fujimoto, and D. Huang, "Quantitative optical coherence tomography angiography of choroidal neovascularization in age-related macular degeneration," Ophthalmology **121**(7), 1435–1444 (2014).
8. L. Liu, S. S. Gao, S. T. Bailey, D. Huang, D. Li, and Y. Jia, "Automated choroidal neovascularization detection algorithm for optical coherence tomography angiography," Biomed. Opt. Express **6**(9), 3564–3576 (2015).
9. K. K. Dansingani, J. Naysan, and K. B. Freund, "En face OCT angiography demonstrates flow in early type 3 neovascularization (retinal angiomatous proliferation)," Eye (Lond.) **29**(5), 703–706 (2015).
10. T. S. Hwang, S. S. Gao, L. Liu, A. K. Lauer, S. T. Bailey, C. J. Flaxel, D. J. Wilson, D. Huang, and Y. Jia, "Automated Quantification of Macular Ischemia Using Optical Coherence Tomography Angiography in Diabetic Retinopathy," JAMA Ophthalmol. In press.
11. D. Huang, Y. Jia, and S. S. Gao, "Principles of Optical Coherence Tomography Angiography " in *OCT Angiography Atlas*, H. D. Lumbros B, Rosenfield P, Chen C, Rispoli M, Romano A, ed. (Jaypee Brothers Medical Publishers, New Delhi, 2015).

12. B. Braaf, K. V. Vienola, C. K. Sheehy, Q. Yang, K. A. Vermeer, P. Tiruveedhula, D. W. Arathorn, A. Roorda, and J. F. de Boer, "Real-time eye motion correction in phase-resolved OCT angiography with tracking SLO," Biomed. Opt. Express **4**(1), 51–65 (2013).
13. T. E. de Carlo, A. Romano, N. K. Waheed, and J. S. Duker, "A review of optical coherence tomography angiography (OCTA)," Int. J. Ret. Vit. **1**(1), 5 (2015).
14. R. F. Spaide, J. M. Klancnik, Jr., and M. J. Cooney, "Retinal vascular layers in macular telangiectasia type 2 imaged by optical coherence tomographic angiography," JAMA Ophthalmol. **133**(1), 66–73 (2015).
15. H. C. Hendargo, R. Estrada, S. J. Chiu, C. Tomasi, S. Farsiu, and J. A. Izatt, "Automated non-rigid registration and mosaicing for robust imaging of distinct retinal capillary beds using speckle variance optical coherence tomography," Biomed. Opt. Express **4**(6), 803–821 (2013).
16. Y. Huang, Q. Zhang, and R. K. Wang, "Efficient method to suppress artifacts caused by tissue hyper-reflections in optical microangiography of retina in vivo," Biomed. Opt. Express **6**(4), 1195–1208 (2015).
17. R. F. Spaide, J. G. Fujimoto, and N. K. Waheed, "Image artifacts in optical coherence tomography angiography," Retina **35**(11), 2163–2180 (2015).
18. D. Pascolini, S. P. Mariotti, G. P. Pokharel, R. Pararajasegaram, D. Etya'ale, A. D. Négrel, and S. Resnikoff, "2002 global update of available data on visual impairment: a compilation of population-based prevalence studies," Ophthalmic Epidemiol. **11**(2), 67–115 (2004).
19. N. Congdon, B. O'Colmain, C. C. Klaver, R. Klein, B. Muñoz, D. S. Friedman, J. Kempen, H. R. Taylor, and P. Mitchell; Eye Diseases Prevalence Research Group, "Causes and prevalence of visual impairment among adults in the United States," Arch. Ophthalmol. **122**(4), 477–485 (2004).
20. F. L. Ferris 3rd, S. L. Fine, and L. Hyman, "Age-related macular degeneration and blindness due to neovascular maculopathy," Arch. Ophthalmol. **102**(11), 1640–1642 (1984).
21. A. Zhang, Q. Zhang, and R. K. Wang, "Minimizing projection artifacts for accurate presentation of choroidal neovascularization in OCT micro-angiography," Biomed. Opt. Express **6**(10), 4130–4143 (2015).
22. D. Huang, Y. Jia, and S. S. Gao, "Interpretation of Optical Coherence Tomography Angiography," in *OCT Angiography Atlas*, H. D. Lumbros B, Rosenfield P, Chen C, Rispoli M, Romano A, ed. (Jaypee Brothers Medical Publishers, New Delhi, 2015).
23. G. Chan, C. Balaratnasingam, P. K. Yu, W. H. Morgan, I. L. McAllister, S. J. Cringle, and D. Y. Yu, "Quantitative Morphometry of Perifoveal Capillary Networks in the Human Retina," Invest. Ophthalmol. Vis. Sci. **53**(9), 5502–5514 (2012).
24. K. Kurokawa, K. Sasaki, S. Makita, Y.-J. Hong, and Y. Yasuno, "Three-dimensional retinal and choroidal capillary imaging by power Doppler optical coherence angiography with adaptive optics," Opt. Express **20**(20), 22796–22812 (2012).
25. M. F. Kraus, B. Potsaid, M. A. Mayer, R. Bock, B. Baumann, J. J. Liu, J. Hornegger, and J. G. Fujimoto, "Motion correction in optical coherence tomography volumes on a per A-scan basis using orthogonal scan patterns," Biomed. Opt. Express **3**(6), 1182–1199 (2012).
26. M. F. Kraus, J. J. Liu, J. Schottenhamml, C.-L. Chen, A. Budai, L. Branchini, T. Ko, H. Ishikawa, G. Wollstein, J. Schuman, J. S. Duker, J. G. Fujimoto, and J. Hornegger, "Quantitative 3D-OCT motion correction with tilt and illumination correction, robust similarity measure and regularization," Biomed. Opt. Express **5**(8), 2591–2613 (2014).
27. L. Liu, Y. Jia, H. L. Takusagawa, A. D. Pechauer, B. Edmunds, L. Lombardi, E. Davis, J. C. Morrison, and D. Huang, "Optical coherence tomography angiography of the peripapillary retina in glaucoma," JAMA Ophthalmol. **133**(9), 1045–1052 (2015).
28. S. S. Gao, G. Liu, D. Huang, and Y. Jia, "Optimization of the split-spectrum amplitude-decorrelation angiography algorithm on a spectral optical coherence tomography system," Opt. Lett. **40**(10), 2305–2308 (2015).
29. M. Zhang, J. Wang, A. D. Pechauer, T. S. Hwang, S. S. Gao, L. Liu, L. Liu, S. T. Bailey, D. J. Wilson, D. Huang, and Y. Jia, "Advanced image processing for optical coherence tomographic angiography of macular diseases," Biomed. Opt. Express **6**(12), 4661–4675 (2015).
30. J. W. Wallis, T. R. Miller, C. A. Lerner, and E. C. Kleerup, "Three-dimensional display in nuclear medicine," IEEE Trans. Med. Imaging **8**(4), 297–330 (1989).
31. D. M. Snodderly and R. S. Weinhaus, "Retinal vasculature of the fovea of the squirrel monkey, Saimiri sciureus: Three-dimensional architecture, visual screening, and relationships to the neuronal layers," J. Comp. Neurol. **297**(1), 145–163 (1990).
32. D. M. Snodderly, R. S. Weinhaus, and J. C. Choi, "Neural-vascular relationships in central retina of macaque monkeys (Macaca fascicularis)," J. Neurosci. **12**(4), 1169–1193 (1992).
33. R. F. Gariano, M. L. Iruela-Arispe, and A. E. Hendrickson, "Vascular development in primate retina: comparison of laminar plexus formation in monkey and human," Invest. Ophthalmol. Vis. Sci. **35**(9), 3442–3455 (1994).
34. P. E. Z. Tan, P. K. Yu, C. Balaratnasingam, S. J. Cringle, W. H. Morgan, I. L. McAllister, and D. Y. Yu, "Quantitative Confocal Imaging of the Retinal Microvasculature in the Human Retina," Invest. Ophthalmol. Vis. Sci. **53**(9), 5728–5736 (2012).
35. K. Pearson, "Note on regression and inheritance in the case of two parents," Proc. R. Soc. Lond. **58**(-1), 240–242 (1895).

36. S. M. McClintic, Y. Jia, D. Huang, and S. T. Bailey, "Optical coherence tomographic angiography of choroidal neovascularization associated with central serous chorioretinopathy," JAMA Ophthalmol. **133**(10), 1212–1214 (2015).
37. N. V. Palejwala, Y. Jia, S. S. Gao, L. Liu, C. J. Flaxel, T. S. Hwang, A. K. Lauer, D. J. Wilson, D. Huang, and S. T. Bailey, "Detection of non-exudative choroidal neovascularization in age-related macular degeneration with optical coherence tomography angiography," Retina **35**(11), 2204–2211 (2015).
38. D. Huang, Y. Jia, M. Rispoli, O. Tan, and B. Lumbroso, "Optical coherence tomography angiography of time course of choroidal neovascularization in response to anti-angiogenic treatment," Retina **35**(11), 2260–2264 (2015).

Introduction

Optical coherence tomographic angiography (OCT-A) employs the motion of blood cells as intrinsic contrast, providing high-resolution maps of microvascular networks in addition to the conventional structural OCT images [1–3]. OCT-A eliminates the risk and reduces the time associated with dye injections [4, 5], making it more accessible for clinical use than fluorescein angiography (FA) or indocyanine green (ICG) angiography, and allowing for better visualization of retinal capillaries.

Another important advantage of OCT angiography over traditional dye-based angiography is the 3-dimensional nature of OCT. By segmenting various tissue slabs (layers), one can generate *en face* OCT angiograms that distinguish between the normal retinal circulation and choroidal circulation, and highlights abnormal neovascularization in the vitreous or outer retinal slabs [6–10]. However, the visualization of deeper vascular networks is impeded by a shadowgraphic flow projection artifact, which comes from fluctuating shadows cast by flowing blood cells in the more superficial vessels. The shadowgraphic projection results in variation of both amplitude and phase, and can be picked up by most OCT angiography algorithms as false flow, also called projection artifact (Fig. 1(A), Fig. 2(A)) [8, 11]. On cross-sectional angiograms, the projection artifact appears as elongated flow signals (tails) below blood vessels, which effectively reduces the depth resolution of OCT angiography. On *en face* angiograms, the projection artifact causes superficial vascular networks to be duplicated on deeper slabs. One clinical problem caused by this artifact is the duplication of normal inner retinal vascular pattern onto the outer retinal slab, which clutters the deeper slab and interferes with the detection and measurement of choroidal neovascularization (CNV) [9, 12–17]. Since CNV is the most serious complication of age-related neovascularization (AMD), the leading cause of blindness in the US [18–20], the flow projection artifact is a problem of great clinical significance.

In commercial OCT angiography and previous work, the flow projection artifact was suppressed with a slab-subtraction (SS) algorithm. For example, the vascular pattern of the inner retinal circulation can be subtracted from the outer retinal slab, leaving the outer retinal slab vessel-free as it should be, physiologically [8, 21]. Unfortunately, the SS algorithm replaces the flow projection artifact with a shadow artifact, the problem of which becomes obvious when one examines a CNV case. The SS algorithm erases most of the CNV that overlaps with the more superficial retinal circulation, leaving gaps that are difficult to reconstruct [22].

Another shortcoming of the SS algorithm is that it does not suppress flow projection within the slab, leaving the obvious tail artifacts on cross-sectional OCT angiograms. Therefore, one cannot use it to delineate separate vascular plexuses without pre-defining their slab boundaries. Previous histological studies have shown that there are as many as 3 distinct vascular plexuses in the inner retina alone [23]. It is difficult to delineate these 3 plexuses *in vivo* using the SS algorithm.

In this work, we present an improved method to solve the projection artifact problem, called the projection-resolved (PR) algorithm. The PR algorithm can identify multiple vessels along an OCT axial scan (A-scan) without presuming a pre-defined slab boundary or the number of slabs and vessels.

We will show that, unlike the SS algorithm, PR preserves the integrity and continuity of deeper vascular networks (e.g. CNV). Furthermore, PR removes tails on cross-sectional OCT angiograms. This allows for the clear visualization of 3 distinct retinal vascular plexuses that previously could only be seen in ex vivo tissue preparations or using adaptive optics [24].

2. Data acquisition

The OCT-A data was acquired using a commercial spectral-domain OCT instrument (RTVue-XR Avanti; Optovue, Inc., Fremont, CA) that has a center wavelength of 840 nm with a full-width half-maximum bandwidth of 45 nm and an axial scan rate of 70 kHz. Angiography scans were performed using the resident AngioVue software. The 3D volumetric angiography scans consisted of a 3 × 3 mm area with a 1.6 mm depth (304 × 304 × 512 voxels). In the fast transverse scanning direction, 304 A-lines were sampled. Two repeated B-scans were captured at a fixed position before proceeding to the next location. A total of 304 locations along a 3 mm distance in the slow transverse direction were sampled to form a 3D data cube. All 608 B-scans in each data cube were acquired in 2.9 seconds. Two volumetric raster scans, one x-fast scan and one y-fast scan, were acquired, registered [25, 26], and merged into one 3D angiogram. Blood flow is detected using the AngioVue software, a commercial version of the split-spectrum amplitude-decorrelation angiography (SSADA) algorithm [1, 27]. The SSADA algorithm calculates the signal amplitude-decorrelation between two consecutive B-scans of the same location. Decorrelation is a function of scatters (red blood cells) displacement over time, representing blood flow signals for OCT-A. The SSADA algorithm splits the OCT spectrum to obtain multiple B-frame images from each B-scan. The split B-frames have longer axial coherence gate, which reduces noise from axial bulk motion. Because the spectral splits are associated with independent speckle patterns, they provide independent flow signal from their respective speckle decorrelation images. Averaging the decorrelation signals from the spectral splits enhances the signal-to-noise ratio of flow detection by up to fourfold [1, 28].

The volume data are segmented using directional graph search [29], which gives boundaries separating the inner limiting membrane (ILM), inner plexiform layer (IPL), inner nuclear layer (INL), outer plexiform layer (OPL), outer nuclear layer (ONL), photoreceptor inner/outer segment (IS/OS) junction (sometimes referred to as ellipsoid zone), retinal pigment epithelium (RPE), and Bruch's membrane (BM). *En face* angiograms are constructed by maximum flow projection within slabs that are defined by the segmented boundaries. The inner retinal slab include layers between the ILM and OPL, and the outer retinal slab includes layers between the ONL and BM. Color composite *en face* OCT angiograms are generated using the top-view technique [1–3, 30] with the more superficial (inner, proximal) slab is placed on top of deeper slabs, thus providing 3D information on a 2D display [1, 29].

3. Theory

Shadowgraphic projection artifacts are demonstrated in Fig. 1 and Fig. 2(A). Shadowgraphic projection is intensity dependent. This is demonstrated by the fact that the low projection values are located on the layers with low OCT intensity signals, such as INL and ONL, and high projection values are located on the layers with high intensity signals, such as IS/OS and RPE. We investigated A-lines with only a single retinal vessel (Fig. 1(B)) and confirmed that the projected flow (decorrelation) values in the outer retina scaled with logarithmic amplitude values. This dependence was removed by normalizing decorrelation D with log amplitude OCT signal S:

$$F = \frac{D}{S} \qquad (1)$$

The log amplitude OCT signal S is the integer output of the RTVue-XR OCT system that is logarithmically related to the reflectance amplitude R. We have established the relationship between S and R by optical bench measurements:

$$R = 6.88 \times 10^{-7} \times 10^{\frac{S}{800}} \tag{2}$$

Using the normalized flow signal F, we found that the projected flow signals were almost always weaker compared to the *in situ* flow signals (Fig. 1(C)). Based on this observation, by searching for successive higher peaks in F values along each A-line from the shallow end (index $i = 1$, e.g. top of Fig. 2(A)) to the deep end (increasing i, e.g. to bottom of Fig. 2(A)), the algorithm effectively identified the real vessels and rejected the projection artifacts (Fig. 2). The PR algorithm keeps the decorrelation values at the successive peak position (real vessels) and set the rest to zero according to Eq. (3) below.

$$C_n = \begin{cases} D_n & , \quad \text{if } F_n > (1+\alpha)\max(F_i), 1 \le i \le n-1 \\ 0 & , \qquad\qquad \text{otherwise} \end{cases} \tag{3}$$

Here i and n are the index of a voxel in an A-line from the shallow (inner, proximal) end. C is the PR-corrected decorrelation values. Note that a small factor α was included to account for noise. We set α as 0.1 for all the processing in this article. The processing time of PR on an A-line is linear to n. For a volume scan of 304 × 304 A-lines, and $n = 512$ pixels per A-line. The processing takes about 10 seconds.
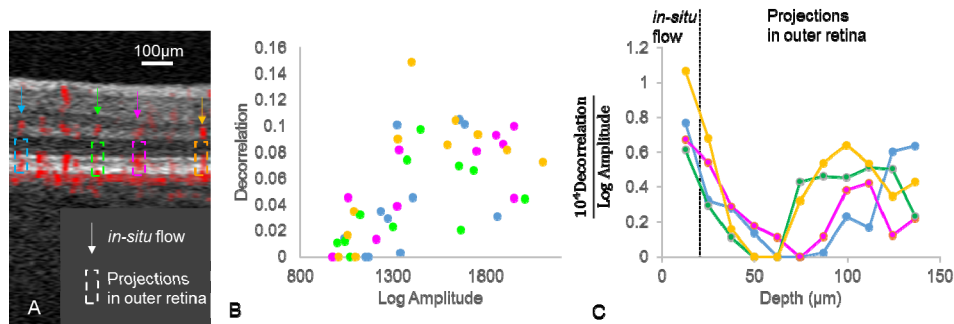

Fig. 1. Illustration of projection artifacts in optical coherence tomographic angiography (OCT-A). (A) Composite cross-sectional OCT-A before projection suppression. The decorrelation signal (red) is overlaid on the structural OCT. The projection artifacts are notable as tails (vertical red streaks) trailing below the real vessels and projected onto deeper high-reflectance layers. (B) Decorrelation values of projected flow are plotted v.s. log amplitude OCT signal. These four sets of projection artifact data chosen are from A-lines that had only one dominant *in situ* flow in the deep retinal plexus (arrows in Panel A. Their tails (rectangles in Panel A) are clearly projection artifacts because we know the outer retina is normally avascular. (C) Plots of the decorrelation adjusted by log amplitude. After the adjustment, the projected flow values are always smaller than the *in situ* flow.

The PR algorithm effectively removes tail artifacts from retinal vessels and recovers accurate information on their axial position (Fig. 2). The resulting PR OCT-A cross-sectional angiograms in the macular region reveal 3 distinct vascular plexuses in the inner retina.
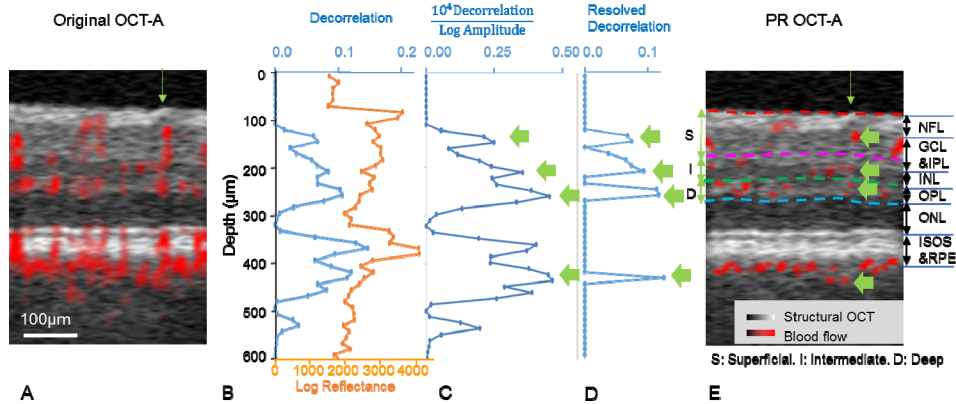
Fig. 2. Illustration of projection-resolved (PR) OCT-A algorithm. (A) Composite cross-sectional OCT-A before projection suppression. This 0.23 mm wide example is taken from the parafoveal region. (B) Original decorrelation and log amplitude values of the A-line pointed to by the green arrow in A. (C) Decorrelation normalized by log amplitude according to Eq. (1). Four successively higher peaks (green arrows) on this plot represent *in situ* flow in real vessels. (D) Decorrelations plot after clean up by the PR algorithm – decorrelation values outside the successive peaks represented projection artifacts and were set to zero (Eq. (3). (E) Composite cross-sectional OCT-A after clean-up of projection artifacts using the PR algorithm. The green arrows in pointed at the same voxels identified as real vessels in C and D. Note that 4 vessels co-existing along the same A-line could be identified on the PR OCT-A, and their axial positions could be pinpointed. The PR OCT-A of the macula shows 3 distinct vascular plexuses in the inner retina - superficial, intermediate, and deep – as has been described in previous histological studies [23].

4. Comparison and evaluation

4.1 Study population

We tested PR OCT-A in 13 healthy study participants (one eye each), whose age ranged from 25 to 58 years. One participant with neovascular age-related macular degeneration confirmed by clinical examination and fluorescein angiography was also used to demonstrate the visualization of CNV. Participants were enrolled after informed consent in accordance with an Institutional Review Board/Ethics Committee-approved protocol at Oregon Health & Science University and in compliance with the Declaration of Helsinki. The data are processed using Casey Reading Center software [29].

4.2 Enhanced depth resolution revealing 3 retinal plexuses

In clinical OCT-A, the retinal circulation is dominated by the superficial layer and the deeper vascular layers have been difficult to visualize as distinct plexuses. We know from previous histological studies that there are three vascular plexuses in human macula (except in the immediate peripapillary region where there are four) [23, 31–34]. The superficial retinal vascular plexus is in the nerve fiber layer (NFL), ganglion cell layer (GCL), and the superficial portion of the inner plexiform layer (IPL). The intermediate capillary plexus is located at the junction between the IPL and the inner nuclear layer (INL). The deep capillary plexus is located at the junction between the INL and the outer plexiform layer (OPL). These 3 plexuses have been well characterized histologically in non-human primates and recently in human cadaveric eyes [23, 31–34]. However, clinical imaging with FA was unable to resolve the 3 plexuses due to lack of depth resolution.

In this section, we compare the results of depth-resolved OCT-A without projection suppression, and then with projection suppression using 2 different methods. For the purpose of OCT image segmentation, we set the automated image processing software to define the intermediate plexuses as the slab 25 μm above to 25 μm below the IPL/INL boundary. The

deep plexus ends at the deep boundary of the outer plexiform layer (OPL). The outer retinal slab was defined as including outer nuclear layer (ONL), photoreceptor layer, the retinal pigment epithelium (RPE), and ending at the Bruch's membrane (BM). *En face* OCT angiograms were obtained using maximum flow projection within these segmented slabs [4].

While OCT has good depth resolution, this resolution was degraded in OCT-A by the projection artifact, which cause images of deeper slabs to be dominated by projected flow. On the cross-sectional angiogram (Fig. 2), this means the superficial retinal vessels have long tails that streak vertically down all the retinal layers and even into the choroid. On the *en face* angiograms of the deeper plexuses and the outer retina (Fig. 3), the projected flow from the superficial plexus predominates, making the capillary plexuses difficult to recognize and cluttering the normally avascular outer retinal slab.

The standard slab-subtraction (SS) method, the maximum projected flow from the more superficial slab is subtracted from the current slab. We implemented the SS algorithm using Eq. (4) below:

$$C_{\text{slab2}} = \begin{cases} D_{\text{slab2}} - D_{\text{slab1}} & , \quad \text{if } D_{\text{slab2}} > D_{\text{slab1}} \\ 0 & , \qquad \text{otherwise} \end{cases} \qquad (4)$$

where D_{slab2} is the decorrelation value from maximum flow projection within the slab of interest, D_{slab1} is the maximum flow projection of all layers above D_{slab2}, and C_{slab2} is the resulting decorrelation value of the SS OCT-A. The SS algorithm effectively removed most projection artifacts from the deeper plexuses and the outer retinal, but unfortunately left shadowing artifacts in its place. This meant the capillaries in the intermediate and deep plexuses (Fig. 3, middle column) become severely fragmented and no longer recognizable as continuous networks. The SS OCT-A images also appear dimmer because subtraction lowered the decorrelation values.

Using PR OCT-A, we are now able to visualize the distinct vascular patterns in the 3 retinal plexuses (Fig. 3, right column). The cross-sectional angiogram shows vessels without tails, so that their axial locations could be pinpointed. There are concentrations of vessels at the level of the intermediate and deep plexuses. The projection artifacts in the outer retina are largely eliminated, but scattered residual artifact remains at the level of the RPE. The *en face* angiograms show that the superficial plexus contain both large and small vessels in a centripetal branching pattern that ends at the foveal circle. The intermediate and deep plexuses are purely composed of capillaries in maze-like networks. Although these 2 plexuses have similar texture, their patterns are not the same when examined in detail. In the deep plexus, there was still some shadowing under the largest vessels from the superficial plexus. Thus the PR algorithm does not perfectly preserve vascular continuity there. But the improvement over SS is dramatic.
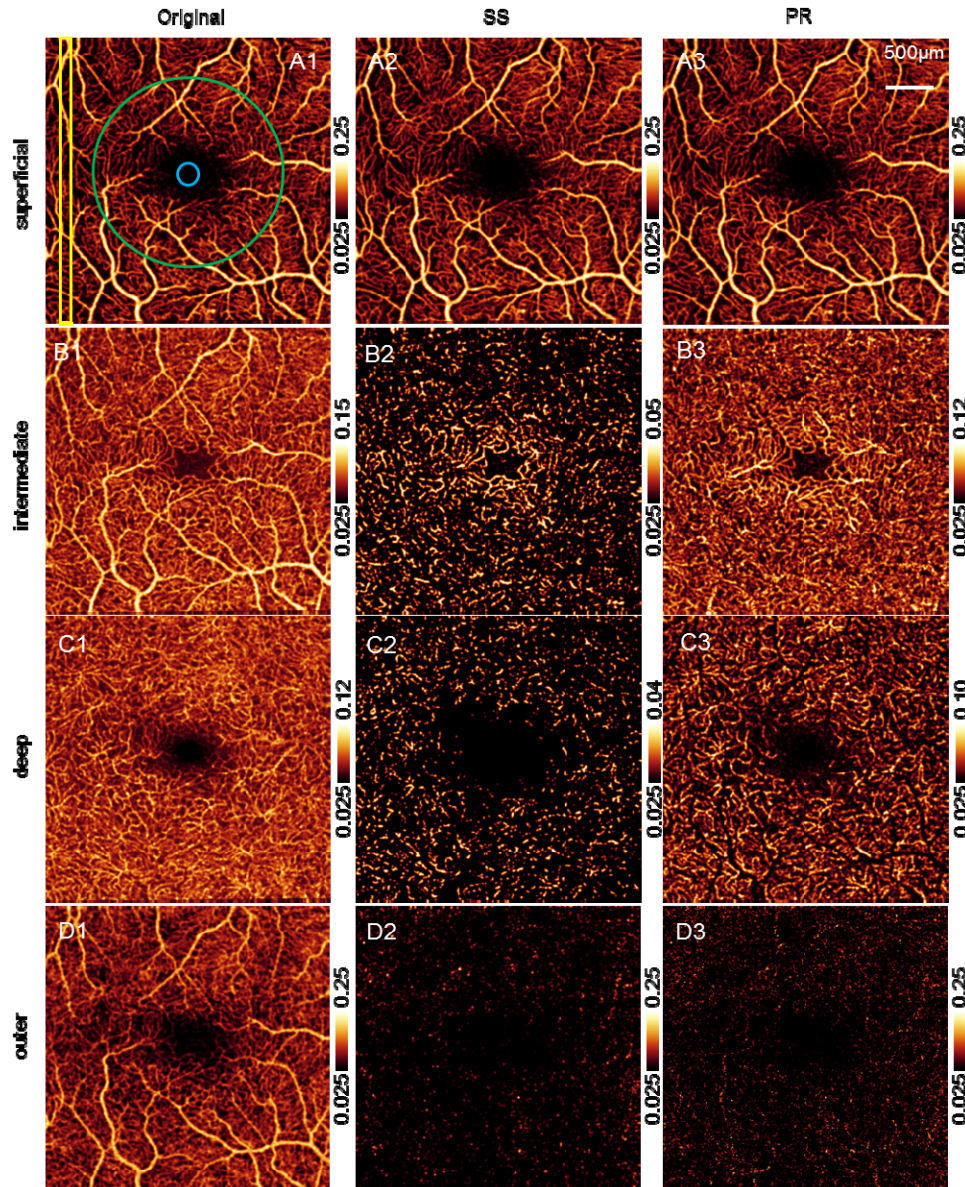
Fig. 3. A comparison of Retinal OCT-A processed without projection suppression (Original, Column 1), with projection suppressed by the standard slab-subtraction method (SS, Column 2), and with the novel projection-resolved algorithm (PR, Column 3). Row A: *En face* OCT-A of the superficial vascular plexus. Row B: *En face* OCT-A of the intermediate capillary plexus. Row C: *En face* OCT-A of the deep capillary plexus. Row D: *En face* OCT-A of the outer retinal slab. In B1, the yellow rectangular is the ROI of the analysis in Fig. 5. The circles mark the parafoveal ROI of the vessel density calculation in Fig. 7.

The PR algorithm produces a truly 3D OCT-A. The fly-through video (Fig. 4(A)) shows that without projection suppression, the superficial vascular pattern is duplicated several times as one flies through deeper reflective layers. In contrast, PR OCT-A shows the distinct patterns characteristic of the various retinal and choroidal plexuses.
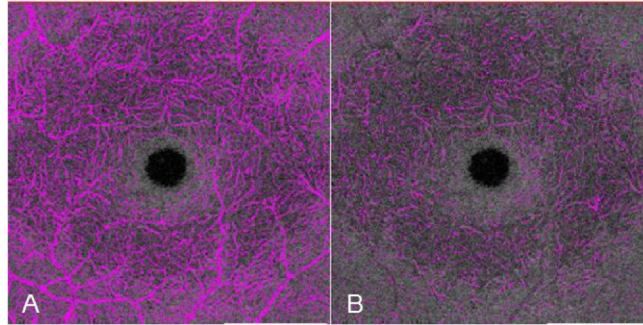
Fig. 4. An *en face* fly-through (superficial to deep) video (Visualization 1) showing 3D OCT-A without projection suppression (A) and with projection artifacts removed using the PR algorithm (B).

To quantitatively confirm that 3 retinal plexuses could be observed in PR OCT-A, we registered all A-lines from the 13 healthy eyes at the segmented IPL/INL boundary [29] within a 3×0.1 mm region of interest (ROI) in the temporal perifoveal area defined by the narrow rectangle in Fig. 3(A1). The vessel densities were calculated as a function of depth in 12.5 μm increments (Fig. 5). Without projection suppression, the vessel density appeared to reach higher plateaus at the IPL and OPL, presumably due to accumulation of projected flow in the relatively high reflectance plexiform layers. But there were no clear peaks. In contrast, the PR OCT-A showed 3 sharp peaks of vessel density corresponding to the 3 retinal vascular plexuses (Fig. 5). The superficial plexus peaks within the GCL. The intermediate plexus peaks at the IPL/INL junction, with valleys 25 μm on each side. The deep plexus peaks at the INL/OPL junction and terminates before reaching the ONL. This pattern was present in all 13 study participants.
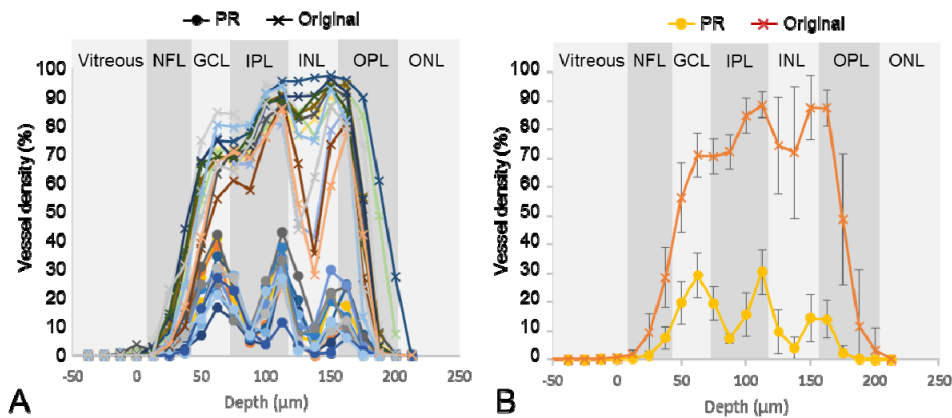

Fig. 5. Plots of retinal vessel density as a function of depth computed from OCT-A with and without projection removal using the PR algorithm. The ROI in a 3×0.1 mm temporal perifoveal location was defined in Fig. (3A1) (yellow rectangle). (A) Individual plots from 13 healthy human study participants. (B) Plot of population mean and standard deviation.

4.3 Vascular pattern similarity as a measure of projection artifact suppression

Without projection suppression, the vascular pattern in overlying layers is duplicated in all deeper angiogram slabs. Thus *en face* OCT-A in deeper slabs would all appear to have patterns similar to the slabs above them. Successful projection suppression should reduce this similarity as much as possible. To evaluate the performance of projection suppression, we use Pearson's product-moment correlation coefficient [35] to quantify the similarity between

vascular patterns in the deeper *en face* OCT-A slabs in comparison to the vascular pattern in the aggregate slab of all layers above. The Pearson correlation coefficient r is calculated according to Eq. (5) below:

$$r = \frac{\sum_{i=1}^{n}(x_i - \bar{x})(y_i - \bar{y})}{\sqrt{\sum_{i=1}^{n}(x_i - \bar{x})^2}\sqrt{\sum_{i=1}^{n}(y_i - \bar{y})^2}} \tag{5}$$

where i is the index of pixels within the *en face* angiogram and $n = 304^2$ is the total number of pixels. x represents the decorrelation values of the deeper slab obtained by maximum flow projection and y represent the decorrelation values of the more superficial slab containing all layers above. $\bar{x}$ and $\bar{y}$ represent the respective slab averages.

$$\bar{x} = \frac{1}{n}\sum_{i=1}^{n} x_i \tag{6}$$

Pearson's r takes values between -1 and 1. A r value close to 1 represents strong positive correlation (similarity), 0 represents no correlation, and values close to -1 represents negative correlation. Note that the Pearson's correlation coefficient is insensitive to brightness and contrast variation or manipulations.

This method was applied to OCT-A from the 13 healthy participants (Fig. 6). Correlation for the intermediate plexus slab was calculated relative to the superficial plexus. Correlation for the deep plexus was calculated relative to the aggregate slab containing both the superficial and intermediate plexus. And correlation for the outer retinal slab was calculated relative to the aggregate slab containing all 3 plexus in the inner retina.

Without projection suppression, r was greater than 0.44 for all 3 deeper slabs, indicating strong projection artifacts (Fig. 6). The standard SS algorithm produced negative r between -0.2 and -0.3 (Fig. 6), which must be due to the fact that it produced shadows where there were overlying flow signals (Fig. 3, middle column). The novel PR algorithm successfully suppressed projection in intermediate plexus and outer retinal slabs, with r within 0.1 of zero (Fig. 6). For the deep plexus, the PR algorithm produced a small negative correlation of -0.2 indicating a small degree of shadowing artifact (Fig. 3(C3)).
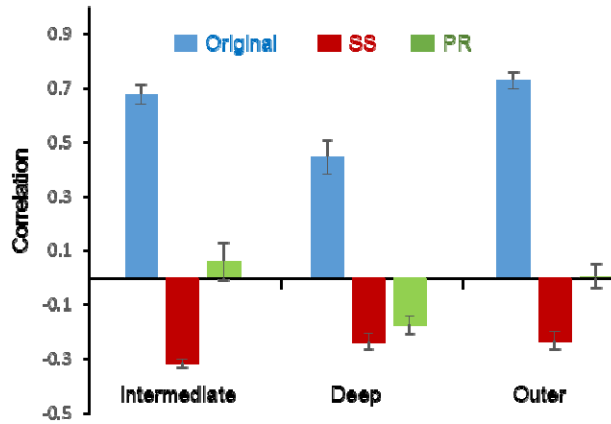

Fig. 6. Correlation of the *en face* angiogram of the deeper slabs – intermediate plexus, deep plexus, and outer retina relative to the all layers above them. The differences between the original, SS, and PR OCT-A were statistically significant for all 3 slabs (p < 0.001 by paired t tests).

4.4 Preservation of vascular continuity

A successful projection suppression algorithm should remove as much projection artifact as possible, but should also preserve as much in situ flow signal (real vessels) as possible. To quantify the preservation of flow signal, the retinal vessel density of parafoveal area (annulus between the blue and green circles in Fig. 3(A1)). The vessel density was calculated using a simple noise threshold, suprathreshold pixels on the *en face* angiograms are counted as vessel pixels and the rest as static pixels. The background decorrelation noise was calculated from the retinal angiogram in the foveal avascular zone (inside blue circle in Fig. 3(A1)). The threshold was set at noise mean + 2.33 standard deviations (99 percentile cut-point assuming normal distribution). According the vessel density metric (Fig. 7), the PR algorithm preserved flow signal significantly better than the SS algorithm. This confirmed our qualitative impression from the inspection of the *en face* angiograms (Fig. 3), which showed that the standard SS algorithm fragmented the capillary networks of the intermediate and deep plexuses, while the PR algorithm was able to largely preserve the continuity of the capillary plexuses.

The preservation of vascular integrity is even more important in the visualization of pathologies such as CNV, an abnormal growth of new vessels in the normally avascular outer retinal slab. Strong projection artifacts in the RPE layer make the detection of CNV more difficult by introducing a dense background clutter (Fig. 8(A)). Applying either SS or PR algorithm removes much of the artefactual flow signal and makes the CNV stand out better (Fig. 8). An additional Saliency-based algorithm is further needed to completely remove the background clutter by recognizing its scattered and disconnected texture [8]. The SS + Saliency algorithm was able to recover the CNV network, but the vascular loops are severely fragmented (Fig. 8(C1)). The PR + Saliency algorithm recovered a more continuous CNV with minimal gaps in the network (Fig. 8(C2)). Clean and complete detection of CNV is important for quantification of the CNV vessel area, an important parameter in assessing the effectiveness of anti-vascular endothelial grow factor (VEGF) therapy and the monitoring of recurrent growth that may prompt additional treatment [7, 8, 36].
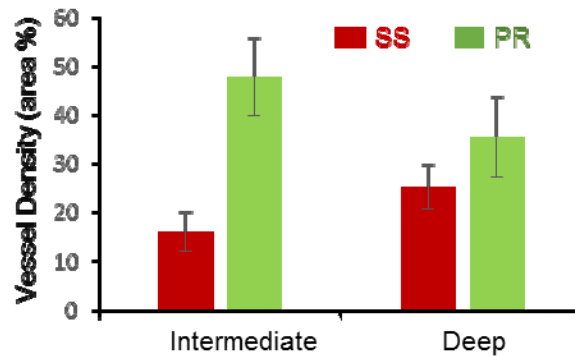

Fig. 7. Comparison of parafoveal vessel density of the intermediate and deep capillary plexuses obtained using SS and PR algorithms. The differences between the 2 algorithms were statistical significant for both plexuses ($p < 0.001$, paired t-test. The ROI location was defined in Fig. 3(A1) (between two blue and green circles).
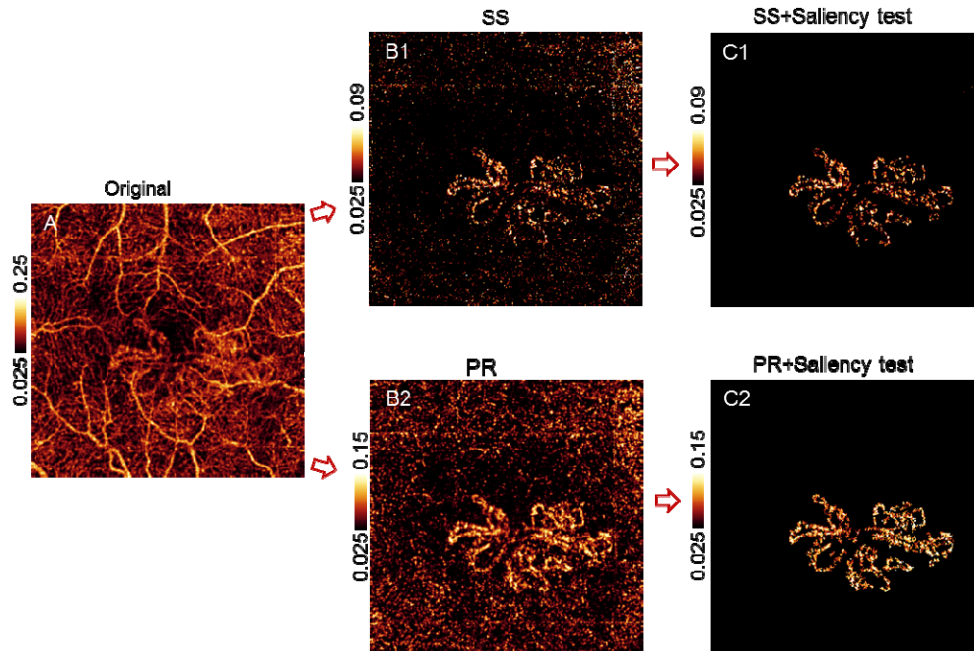
Fig. 8. Comparison of projection artifact suppression algorithms in the visualization of choroidal neovascularization (CNV) in a case of neovascular age-related macular degeneration (AMD). (A) *En face* OCT-A of the outer retinal slab without projection artifact suppression. (B1) Projection suppression with the SS algorithm alone. (B2) projection suppression with the PR algorithm. (C1) A Saliency-based algorithm is used to clean up background clutter after SS. (C2) A Saliency-based algorithm is used to clean up background clutter after PR.

5. Conclusions and discussion

We developed the PR algorithm to more effectively remove the shadowgraphic projection artifact in OCT-A. The results shown here demonstrated that the PR algorithm is able to remove projection artifacts as well as the standard SS algorithm, while minimizing the undesirable side effects of introducing shadowing and leaving gaps in deeper vascular networks.

This novel PR algorithm is uniquely able to identify multiple vessels within a single A-line and allow their depths to be pinpointed on cross-sectional OCT-A. This enhanced depth resolution leads to the visualization of 3 distinct retinal vascular plexuses of the human eye non-invasively and *in vivo,* for the first time in OCT-A. The location of the 3 plexuses agrees with known histology results [23]. The accurate assessment of capillary nonperfusion in the retinal plexuses may be useful in monitoring diabetic retinopathy [6], a leading cause of blindness [19]. The PR algorithm, together with the Saliency algorithm, also more cleanly completely separated CNV flow signal from projected clutter. This ability may improve the early detection of CNV [37] and the management anti-VEGF therapy in neovascular AMD [38], another leading cause of blindness [19].

The PR algorithm is based on 3 novel ideas. One, the projection artifact should be resolved on a voxel-by-voxel basis. This new approach resolves the depth of vessels to the full extent allowable by the available coherence gating. This enhanced depth resolution made it possible for us to establish the depths of the 3 retinal plexuses *in vivo.* Two, the log amplitude of a voxel was taken into account in determining whether the decorrelation was due to *in situ* flow (real blood vessels) or projected flow (artifact). This improved the accuracy of projection resolution. Three, instead of subtracting the maximum decorrelation from overlying voxels in the axial line, we preserved the full decorrelation values of voxels

determined to contain *in situ* flow. This helped preserve the brightness and continuity of deeper vascular networks and reduced the introduction of shadows in place of projection. These 3 elements worked together well in the PR algorithm. Further improvements may be possible using variations on these themes.

To expedite the development of the PR algorithm, we used a simple model to relate the decorrelation value of projected flow with its log amplitude OCT signal and the overlying *in situ* flow. The model assumes that both in situ and projected decorrelation values are influenced by the reflectance amplitude, and the projected flow signal is lower than the in situ flow signal in a linear fashion. This simple model works very well under small vessels, but does not work as well under larger superficial vessels, where it creates some shadow in the deep plexus but leaves some residual projection artifact in the RPE layer. Larger vessels create larger and more variable perturbations in terms of in situ flow, projected flow, in situ reflectance, and distal shadowing. More perfect artifact removal under larger vessels may require a nonlinear, adaptive, or layer-specific approach. A more sophisticated model based on experimental calibration and computational simulation may further improve the PR algorithm. The current PR algorithm remains imperfect, with persistent minor gaps in the processed deep retinal plexus and projected artifacts in the RPE layer that require removal using the Saliency algorithm, further improvements are needed. Nonetheless, the ability to resolve the retinal capillary plexuses in the normal state and choroidal neovascularization in the diseased state without significant flow projection artifact represents a major improvement over the standard SS approach.

Acknowledgments